Long spin coherence and relaxation times in nanodiamonds milled from polycrystalline ^{12}C diamond

James E. March[,1,*] Benjamin D. Wood[,1] Colin J. Stephen,[1] Laura Durán Fervenza[,1]
Ben G. Breeze[,1] Soumen Mandal[,2] Andrew M. Edmonds,[3] Daniel J. Twitchen,[3]
Matthew L. Markham[,3] Oliver A. Williams[,2] and Gavin W. Morley[1]

[1]*Department of Physics, University of Warwick, Coventry CV4 7AL, United Kingdom*

[2]*School of Physics and Astronomy, Cardiff University, Queen's Building, The Parade, Cardiff CF24 3AA,
United Kingdom*

[3]*Element Six Global Innovation Centre, Harwell Oxford, Fermi Avenue, Didcot, Oxfordshire OX11 0QR,
United Kingdom*

The negatively charged nitrogen-vacancy center (NVC) in diamond has been utilized in a wide variety of sensing applications. The long spin coherence and relaxation times (T_2^*, T_2 and T_1) of the center at room temperature are crucial to this, as they often limit sensitivity. Using NVCs in nanodiamonds allows for operations in environments inaccessible to bulk diamond, such as intracellular sensing. We report long spin coherence and relaxation times at room temperature for single NVCs in isotopically purified polycrystalline ball-milled nanodiamonds. Using a spin-locking pulse sequence, we observe spin coherence times, T_2, up to 786 ± 200 µs. We also measure T_2^* times up to 2.06 ± 0.24 µs and T_1 times up to 4.32 ± 0.60 ms. These results represent improvements on the leading literature values for T_2 and T_1 times in nano- and microdiamond and for T_2^* times in nanodiamond. Scanning-electron-microscopy and atomic force microscopy measurements show that the diamond containing the NVC with the longest T_1 time is smaller than 100 nm. EPR measurements give an N_s^0 concentration of 0.15 ± 0.02 parts per million for the nanodiamond sample.

I. INTRODUCTION

The N-V^- center (NVC) has proven to be an effective tool in the fields of magnetometry [1–4], thermometry [5–8], electrometry [9–11], and radio-frequency (rf) field sensing [12,13], amongst other sensing applications. Key properties of the electronic spin-1 system that make it favorable for sensing include optical spin readout, optical initialization into the $m_s = 0$ state, and long spin coherence and relaxation times [14]. Furthermore, as nanodiamonds containing NVCs are biocompatible [15], they show promise for biosensing, including intracellular imaging and sensing techniques [6,16–20].

Of the various sensing methods that the NVC has been applied to, many are limited by one (or more) of the spin-relaxation times of the center: the inhomogeneous relaxation time, T_2^*, the spin coherence time, T_2, and the longitudinal relaxation time, T_1. For example, T_2^* can limit the sensitivities of thermometry [21] and dc magnetometry [1,22], whereas T_1 limits the T_1 relaxometry-measurement sensitivity [23,24]. T_2 is not only a key parameter in many sensing schemes [1,22,25,26] but also in the proposed use of nanodiamonds containing a single NVC for tests of fundamental physics [27–30].

The spin coherence time of the NVC is heavily dependent on its host material. At room temperature, T_1 can be up to 12 ms in bulk diamond [31]. $T_2 = 730$ µs, obtained with a Hahn-echo sequence, has been observed for a single center at room temperature in bulk CVD diamond with natural ^{13}C abundance [32]. This has been extended to $T_2 = 2.4$ ms using dynamical decoupling [32], whereas $T_2 = 1.8$ ms has been measured for a single NVC using a Hahn-echo sequence in isotopically purified ultrapure bulk CVD diamond [33].

Spin coherence and relaxation times in nanodiamond have so far been measured to be significantly shorter. This is thought to be due to interaction with spins on the surface of the nanodiamond, as well as the typically higher nitrogen concentration found in nanodiamond [34–38]. Charge fluctuations on the surface of the diamond have also been shown to affect the coherence times of near-surface NVCs,

*[*]james.march@warwick.ac.uk

including in nanodiamond [39–42]. Surface effects are particularly detrimental to the T_1 of NVCs in nanodiamonds [43,44].

The longest spin coherence time observed in nanodiamond (or microdiamond) to date is 708 µs [45]. This measurement was made on a single NVC in a single-crystal isotopically purified low-nitrogen lithographically fabricated nanopillar. The pillars were 300–500 nm in diameter and 0.5–2 µm in length. A version of these pillars (diameter = 500 nm and length = 2 µm) yielded a single NVC T_2^* time of 6.42 µs [45]. $T_2 = 468$ µs has been demonstrated for single NVCs in smaller, 200 nm diameter, ball-milled nanodiamonds [46]. In a different milled-nanodiamond sample with a mean diameter of 23 nm, T_2^* of 0.44 µs (extended to 1.27 µs using radio waves to drive substitutional-nitrogen groups) has been reported [34]. $T_1 = 1.25$ ms was measured for a single NVC in such a nanodiamond [34]. NVCs in commercial nanodiamonds with diameters of around 100 nm have been found to have T_1 times of 100 µs or less [24]. A summary of the measured T_2^*, T_2 and T_1 for single NVCs in various diamond materials is displayed in Table I.

We present long spin coherence and relaxation times for single NVCs in small, ^{12}C-isotopically purified, ball-milled nanodiamonds. Milling allows for the quick production of a large mass of nanodiamond, as three-dimensional volumes of bulk diamond (e.g., a mass of 0.1 g) can be processed in one go, in contrast to the two-dimensional approach of fabricating pillars. While lithographic fabrication of 300 nm × 500 nm pillars can yield up to 6.3×10^5 pillars from a 500 µm × 500 µm × 500 µm diamond plate [45], ball milling a plate of the same volume can yield up to 10^9 diamonds with diameters of 300 nm. Furthermore, ball milling allows for many (approximately 10–20) larger diamond plates to be milled at once [48], increasing the amount of nanodiamonds that can be produced to the order of 10^{12}. We use ^{12}C-isotopically enriched diamond as our starting material to improve the spin coherence times of the NVCs. ^{13}C, with a natural isotopic abundance in diamond of 1.1%, has a nuclear spin of 1/2 and so is a source of decoherence to the NVC spin [33]. Using spin locking, a pulse scheme shown to have applications including magnetometry [4], rf field sensing [13], paramagnetic spin-bath cooling [49,50], and dynamic nuclear polarization (DNP) [51,52], we observe spin coherence times, T_2, up to 786 ± 200 µs. Furthermore, we report T_1 values up to 4.32 ± 0.60 ms and free-induction-decay T_2^* values up to 2.06 ± 0.24 µs.

II. METHODS

The nanodiamonds used in this study were ball milled with silicon nitride, following the process described in Ref. [48]. The starting material was pieces from the edge of a CVD plate grown by Element Six. The plate was

TABLE I. The T_2^*, T_2, and T_1 times for single NVC defects contained within bulk and nanodiamond for different sizes, purities, and fabrication methods. The T_2 value for Ref. [33] was obtained using a Hahn-echo sequence. The T_2 values displayed for Refs. [45,47] were obtained using a Carr-Purcell-Meiboom-Gill (CPMG) pulse sequence. The T_2 value displayed for Ref. [46] was obtained using an XY8-4 dynamical decoupling sequence. The T_2 value displayed for Ref. [34] was obtained using a universal dynamical decoupling sequence. The T_2 value displayed for this work has been obtained using a spin-locking pulse sequence. For Ref. [32], $T_2 = 730$ µs was obtained using a Hahn-echo sequence and $T_2 = 2400$ µs was obtained using an XY8-4 dynamical decoupling sequence. [N_s] represents the concentration of substitutional nitrogen impurities. HPHT stands for high pressure, high temperature.

Synthesis method	Nanodiamond fabrication method	Size (nm)	[N_s] (ppm)	T_2^* (µs)	T_2 (µs)	T_1 (ms)	Reference
CVD[a]	⋯	Bulk	~10			12	[31]
CVD	⋯	Bulk	0.001–0.005		730, 2400		[32]
CVD[a]	⋯	Bulk	5×10^{-5}		1800		[33]
CVD[a]	Lithography plus etching	300–500	Low[b]	6.42	708		[45]
CVD	SiN ball milled [48]	~200	0.121		468		[46]
CVD	Etching	~50 × 150 pillar	<0.005	1.83	210		[47]
HPHT	Milled	~23	<50	0.44 (1.27)[c]	67	1.25	[34]
CVD[a]	SiN ball milled [48]	~100	0.15	2.06	786	4.32	This work

[a] ^{12}C isotopically purified material.
[b] NVC contained within 6-nm-thick ^{15}N isotopically purified layer, with 100-nm-thick high-purity buffer layers above and below.
[c] $T_2^* = 0.44$ µs was obtained using a typical Ramsey scheme. T_2^* was extended to 1.27 µs by using radio waves to drive substitutional-nitrogen groups.

a single-crystal sample, grown for NVC magnetometry. The material from the edges of the plate, however, was polycrystalline. The sample was not irradiated or annealed.

Measurements on the single NVCs were carried out on a home-built room-temperature confocal fluorescence microscope (CFM) running the QUDI software [53]. The nanodiamonds were deposited onto an n-type silicon wafer with a coordinate system etched into the surface [46]. The coordinate system allowed a specific nanodiamond, investigated on the CFM, to be located using scanning electron microscopy (SEM), in order to measure its dimensions. To deposit the nanodiamonds onto the surface of the wafer, a suspension of nanodiamonds in methanol was sonicated for 30 min before being sprayed into a vial through a nebulizer. The vial, now containing a cloud of nanodiamonds, was upturned over the wafer, allowing the nanodiamonds to fall onto the surface of the silicon. This method was found to give a reasonably even coverage of nanodiamonds across the surface of the wafer.

Microwaves, generated with a Keysight N5172B, were delivered to the NVC via a 20-μm diameter wire, brought within roughly 20 μm of the respective nanodiamond. Only nanodiamonds containing a single NVC were investigated. NVCs were confirmed to be a single center via Hanbury Brown and Twiss (HBT) experiments, where the second-order correlation function, $g^{(2)}(0)$, was below 0.5 in each case [54].

A static magnetic field was applied to the center via a neodymium magnet, positioned such that the direction of the magnetic field was aligned with the nitrogen-vacancy axis. Mounting the magnet on a servo-controlled robotic arm allowed for precise control of the position and orientation of the magnet with respect to the nanodiamond. The field was chosen so that the energy gap between the $m_s = 0$ and $m_s = -1$ sublevels was approximately 2 GHz. This frequency was measured using continuous-wave optically detected magnetic resonance (ODMR) and corresponds to a magnetic field component parallel to the N-V axis, $B_\parallel$, of 31 mT at the NVC.

In a sample where 54 fluorescent sites were examined on the confocal microscope, 16 were confirmed to be single NVCs via HBT experiments. As single NVCs were the subject of this study, there was some selection bias in avoiding particularly bright spots that were likely to contain large numbers of NVCs. It is not known how many nanodiamonds contained zero NVCs, as they do not fluoresce. The centers showed high levels of charge stability, with very few displaying charge-state switching. As this was a nanodiamond sample, the N-V axis can lie in any orientation. However, the robotic arm used for aligning the magnet to the N-V axis has a relatively limited range of motion. Therefore, the specific NVCs selected for spin coherence and relaxation-time measurements were chosen because their N-V axis was in an orientation accessible to our magnetic field.

Five NVCs in five different nanodiamonds were fully characterized in this study. T_2^* was measured for each nanodiamond, as well as three measurements of T_2 using Hahn-echo, XY8-4, and spin-locking pulse sequences. T_1 was also measured for each NVC. The pulse sequences used to perform the measurements are displayed in Fig. 1.

All of the pulse sequences displayed in Fig. 1 begin and end with a 532-nm laser pulse. These are the initialization (into the $m_s = 0$ state) and readout pulses, respectively. Figure 1(a) shows a Ramsey scheme, used to measure the inhomogeneous dephasing time, T_2^*, of the NVC. The T_2^* of a single NVC is primarily governed by slowly varying magnetic and electric fields as well as strain and temperature fluctuations [22]. The Hahn-echo sequence, shown in Fig. 1(b), largely negates these dephasing mechanisms. The π pulse inverts the precession of the spin and so phase accumulated during the first wait period τ is cancelled in the second [22]. This is provided that the time scale on which the noise varies is long compared to τ. The resulting decay constant, T_2, is dominated by magnetic interaction with proximate spins.

In Fig. 1(c), which shows the XY8 sequence, additional refocusing π pulses mitigate the dephasing effects of magnetic noise fluctuating on shorter time scales [55]. The phase switching and time symmetry of the sequence means that the scheme is more resistant to errors in pulse length than, e.g., a Carr-Purcell-Meiboom-Gill (CPMG) sequence [56,57].

Figure 1(d) shows a spin-locking pulse sequence. Also referred to as $T_{1\rho}$ (T_1 in the rotating frame), it is considered to be the upper limit of T_2 that can be measured by a dynamical decoupling sequence, for a given microwave power [31,58]. After initialization into the $m_s = 0$ state, a $(\pi/2)_x$ pulse places the spin of the NVC into an equal superposition of $m_s = 0$ and $m_s = 1$. A long microwave pulse, phase shifted by 90° to the $(\pi/2)_x$ pulse, continuously drives the spin, keeping it aligned along the y axis of the Bloch sphere. The spin state is optically read out following a further $\pi/2$ pulse. Figure 1(e) shows the T_1 sequence.

III. RESULTS

Of the five centers in this study, the longest recorded T_2^*, T_2, and T_1 measurements are displayed in Figs. 2(a)–2(c), respectively. The longest measured T_2 was obtained via the spin-locking pulse sequence. Figure 2(d) shows T_2^*, $T_2^{(HE)}$, $T_2^{(XY8-4)}$, $T_2^{(SL)}$, and T_1 measurements for each of the five NVCs. We find that the same NVC (ND3) yields the longest times for $T_2^{(HE)}$, $T_2^{(XY8-4)}$, and $T_2^{(SL)}$, whereas the longest recorded T_2^* and T_1 were obtained from two other centers (ND5 and ND4, respectively). It was found that spin locking can increase T_2 by up to a factor of 5.7 relative to XY8-4. A sixth single NVC was partially characterized and was found to have $T_2^{(HE)} = 12.4 \pm 0.5$ μs, comparable
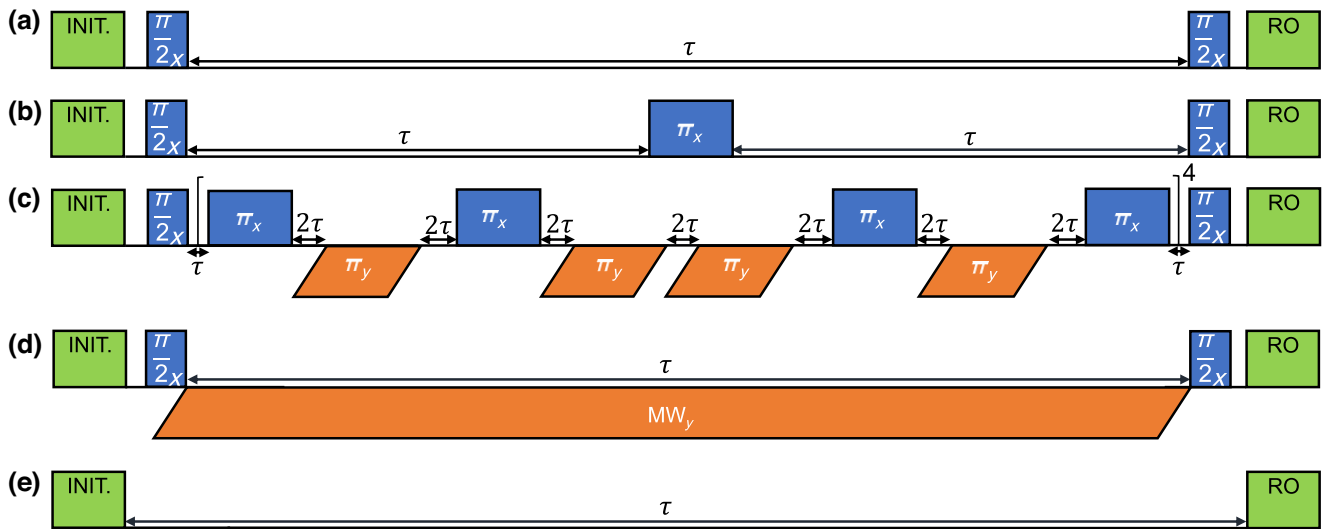
FIG. 1.   A schematic of the five different pulse sequences used in this study. The green block at the beginning and end of each sequence represents the 532-nm laser initialization (INIT.) and readout (RO) pulses, which are identical for each pulse sequence. In practice, the initialization and read out is performed by the same (single) pulse, as the pulse sequence is repeated many times to build up the signal-to-noise ratio. The blue and orange blocks represent x and y microwave (MW) pulses, respectively. (a) The Ramsey sequence, used to measure T_2^*. (b) The Hahn-echo sequence, used to measure T_2. (c) An XY8-4 pulse sequence. The section of eight π pulses repeats four times before the second $\pi/2$ pulse is applied. This sequence was used to measure $T_2^{(\text{XY8-4})}$. (d) The spin-locking pulse sequence, used to measure $T_2^{(\text{SL})}$. (e) The sequence used to measure T_1. Phase cycling was used in sequences (a)–(d) to reject common-mode noise.

to ND1, ND2, and ND3. However, due to a combination of low center fluorescence, low ODMR contrast, and sample drift, it was not possible to make dynamical decoupling measurements at the same microwave power that had been used in measurements on the other five centers or to measure its T_1. No spin measurements were made for any other NVCs from this nanodiamond sample.

Due to the aforementioned coordinate system on which the diamonds were deposited, it was possible to locate and measure the dimensions of ND4 ($T_2^* = 1.71 \pm 0.20$ μs, $T_2^{(\text{SL})} = 759 \pm 100$ μs and $T_1 = 4.32 \pm 0.60$ ms) using atomic force microscopy (AFM) and SEM. The long and short axes of the diamond in the x-y plane were measured to be 80 ± 10 nm and 47 ± 10 nm respectively, as shown in Fig. 3. The height of ND4 was measured, using AFM, to be 7.8 ± 1.1 nm. Therefore, the maximum distance that the NVC can be from a surface of the diamond is less than 5 nm. This is comparable to the dimensions of the diamonds investigated in Ref. [34] and far smaller than those studied in Ref. [45]. Unfortunately, due to a combination of surface contamination and nanodiamond agglomeration, it was not possible to locate any of the other four diamonds referenced in Fig. 2.

IV. DISCUSSION

We believe that the values of $T_2^* = 2.06 \pm 0.24$ μs, $T_2 = 786 \pm 200$ μs and $T_1 = 4.32 \pm 0.6$ ms are the longest

measurements of these three characteristics for an NVC in nanodiamond. Furthermore, 786 ± 200 μs may be longest T_2 reported for any electronic spin system in a nanoparticle. Although $T_2^* = 6.42 \pm 1.05$ μs has been reported for a single NVC in a high-purity fabricated diamond pillar, the diamond was microscale as opposed to nanoscale [45]. Many sensing applications for NVCs in nanodiamond require nanodiamonds with diameters of around 100 nm or less; e.g., those where the diamonds enter cells [59]. As our nanodiamonds were milled rather than etched, we efficiently created large quantities of nanodiamond, on the order of 0.1 g. On a similar note, polycrystalline CVD diamond is easier to grow than single crystal, as well as being cheaper.

Using EPR, the N_s^0 concentration of our sample was measured to be 0.15 ± 0.02 ppm (parts per million), as shown in Fig. 4. For this isotopically purified nanodiamond sample, substitutional-nitrogen impurities dominate dephasing due to intrinsic spins [22,60]. It is expected that the low substitutional-nitrogen concentration of our sample, along with ^{12}C-isotopic purification, are significant factors as to why the T_2^* and T_2 times measured in this work are longer than observed previously in nanodiamonds of a similar size. It has been demonstrated that the spins of either nitrogen or ^{13}C can dominate T_2^* and T_2, depending on their relative concentrations [14,60–63]. In bulk diamond, the expected T_2^* for an NVC ensemble in a sample with <50 ppm substitutional-nitrogen and natural ^{13}C
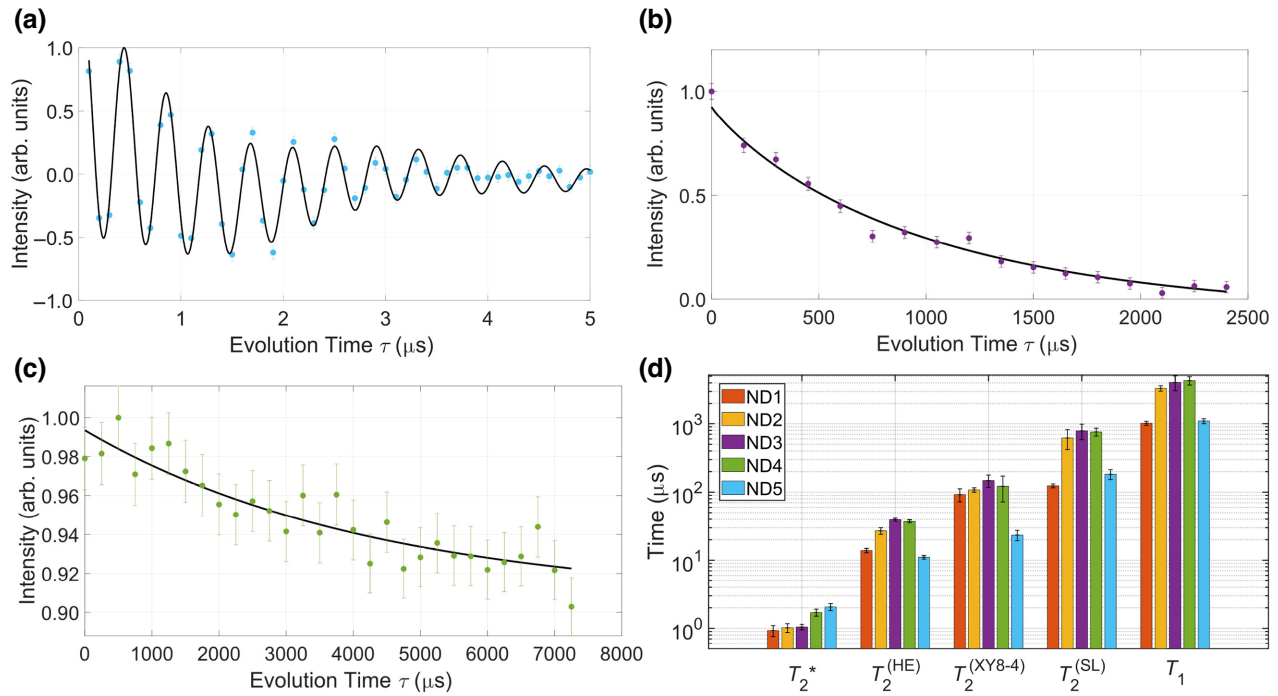
FIG. 2. (a) The Ramsey measurement of the T_2^* coherence time for center ND5 using the pulse sequence shown in Fig. 1(a). $T_2^* = 2.06 \pm 0.24$ μs was extracted from the fit of the form $A + Be^{-(\tau/T_2^*)} \Sigma_k \sin(c_k t + d_k)$ with three frequency components [47]. Phase cycling was used in this measurement to reject common-mode noise and so the plotted signal represents the difference in the photoluminescence-intensity readout signals of the two basis states, $m_s = 0$ and $m_s = -1$. The signal is normalized such that the highest value of the fitted function is equal to 1. (b) The spin-lock measurement of the $T_2^{(SL)}$ coherence time for center ND3 using the pulse sequence shown in Fig. 1(d). A value of $T_2^{(SL)} = 786 \pm 200$ μs was extracted from a fit of the form $A + Be^{-(\tau/T_2)}$ [13]. Phase cycling was used in this measurement to reject common-mode noise and so the y axis represents the difference in the photoluminescence-intensity readout signals of the $m_s = 0$ and $m_s = -1$ states, with the maximum measured difference normalized to 1. (c) Measurement of the T_1 relaxation time for center ND4 using the pulse sequence shown in Fig. 1(e). $T_1 = 4.32 \pm 0.60$ ms was extracted from the exponential fit of the form $A + Be^{-(\tau/T_1)}$. Phase cycling was not used in this measurement and so the y axis represents the decay of the measured photoluminescence intensity after initialization into the $m_s = 0$ state, with the maximum measured intensity normalized to 1. (d) A plot showing the measured values of T_2^*, T_2 (obtained through Hahn-echo, XY8-4, and spin-locking pulse sequences) and T_1 for each of the five NVCs investigated in this study. The mean value for each of the five measured quantities across the five NVCs is as follows: $T_2^* = 1.35 \pm 0.20$ μs, $T_2^{(HE)} = 25.8 \pm 5.2$ μs, $T_2^{(XY8-4)} = 98.7 \pm 19$ μs, $T_2^{(SL)} = 494 \pm 96$ μs, and $T_1 = 2.77 \pm 0.64$ ms.

abundance, as in Ref. [34], is approximately 0.2–0.3 μs [61]. For an ensemble of NVCs in a bulk sample with an extremely low nitrogen concentration but a natural ^{13}C abundance, as in Ref. [47], T_2^* is limited to approximately 1 μs as a result of the ^{13}C nuclear spins [61]. However, for a bulk sample with a 0.15-ppm substitutional-nitrogen concentration and ^{12}C-isotopic enrichment, as in this work, the expected T_2^* is 40–50 μs [61]. This suggests that both isotopic purification and a low substitutional-nitrogen concentration are important factors contributing to the long T_2^* times reported in this work. It also shows that the T_2^* times that we report are not limited by intrinsic spins and so are likely limited by surface effects. It has been demonstrated for NVC ensembles in bulk diamond that both the substitutional-nitrogen concentration and the ^{13}C concentration are inversely proportional to T_2, with nitrogen spins typically dominating dephasing [60,62–64]. This

may explain why the $T_2^{(HE)}$ times reported in this work are between those reported in Refs. [34,47], given that the substitutional-nitrogen concentration of our sample lies between these samples. The substitutional-nitrogen concentration has also been demonstrated to contribute significantly to T_1 relaxation. The impact on T_1 times can be significant at room temperature, where a decrease in nitrogen concentration from approximately 50 ppm to approximately 20 ppm can result in an increase in T_1 by almost a factor of 2 [65]. Therefore, we would expect that the lower nitrogen concentration is a primary reason as to why the NVCs in this work have longer T_1 times than has previously been reported in the literature for centers hosted in nanodiamond.

The magnetic effects of spins, such as dangling bonds, at the diamond surface are considered to be a significant, and possibly dominant, factor as to why T_2^*, T_2, and T_1
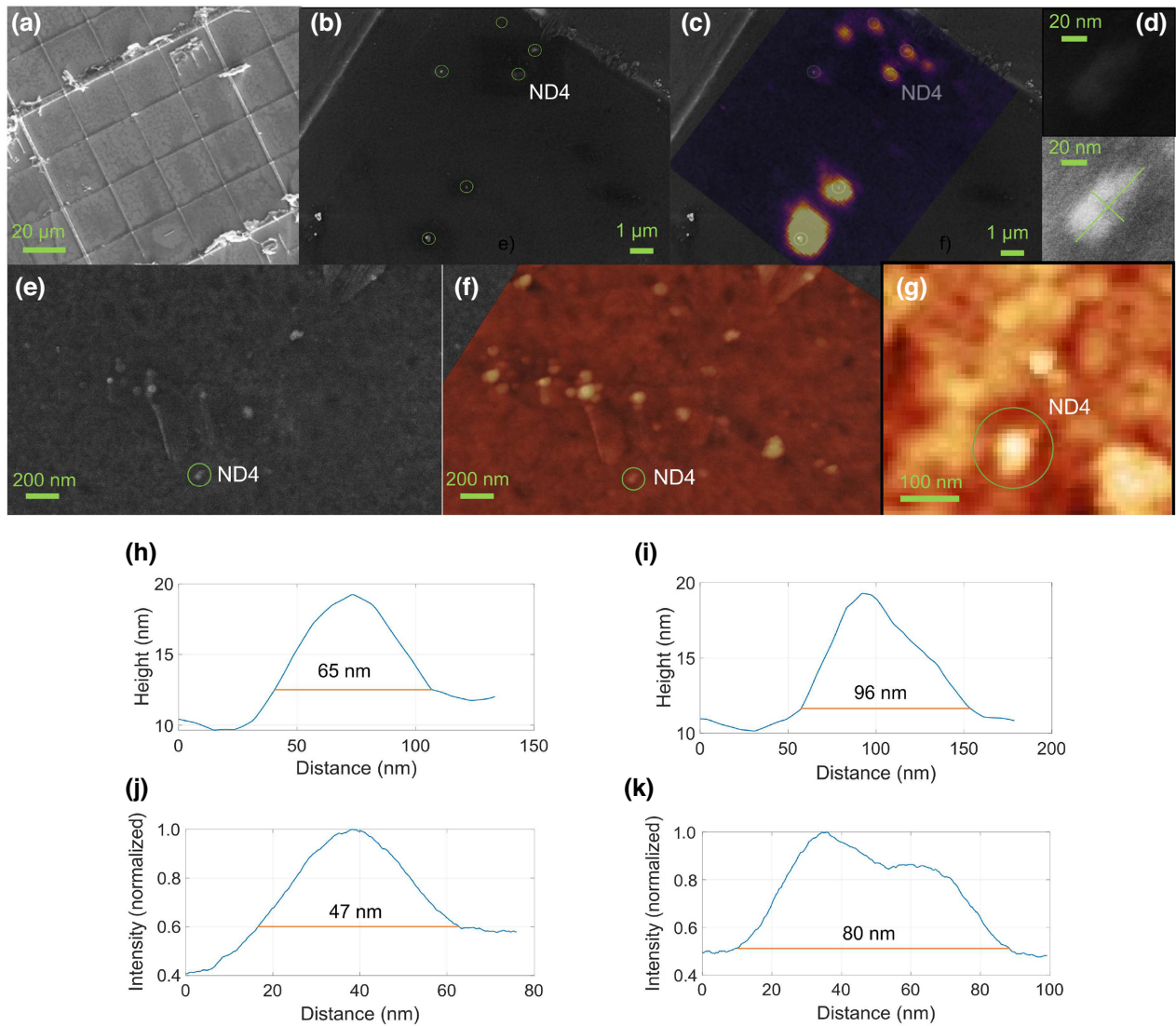
FIG. 3. (a) An SEM image showing the coordinate system on the surface of the silicon wafer. The system allows specific nanodiamonds, known to contain single NVCs from examination on a CFM, to be located using SEM. (b) An SEM image showing the location of ND4. The NVC contained within the highlighted nanodiamond (ND4) had the following spin coherence and relaxation times: $T_2^* = 1.71 \pm 0.20\,\mu s$, $T_2^{(SL)} = 759 \pm 100\,\mu s$ and $T_1 = 4.32 \pm 0.60$ ms. (c) A fluorescence image, taken on a CFM, of the same area as (b), overlaid on (b). This shows how nanodiamonds containing fluorescent NVCs can be located using both SEM and CFM. Filters (532-nm notch and 633-nm high-pass) are used on the CFM to optimize for collection of light emitted from the NVC, which has an optical zero-phonon line at 637 nm [14]. (d) High-magnification images of ND4. The upper image shows the original SEM image, whereas the lower image has been enhanced in ImageJ to allow for easier visualization of its dimensions. The lower image has been enhanced by using the "equalize histogram" function and then applying a Gaussian blur with $\sigma = 1.5$. (e) A high-magnification SEM image showing the location of ND4. (f) An AFM image of the area shown in (e), overlaid over (e), showing the agreement between AFM and SEM images of the area. (g) A high-magnification AFM image of ND4. (h) A plot of the height against the position for the short axis of the diamond in the *x*-*y* plane for the AFM image shown in (g). (i) A plot of the height against the position for the long axis of the diamond in the *x*-*y* plane for the AFM image shown in (g). The surface of the silicon is at a height of 11.5 ± 1.1 nm, giving ND4 a height of 7.8 ± 1.1 nm. (j) A plot of the pixel intensity against the position for the short axis of the diamond in the *x*-*y* plane for an SEM image [shown in (d)]. The length of the short axis is 47 ± 10 nm. (k) A plot of the pixel intensity against the position for the long axis of the diamond in the *x*-*y* plane for an SEM image [as shown in (d)]. The length of the long axis is 80 ± 10 nm. The measurements in the *x*-*y* plane taken from the SEM images are shorter than those taken from the AFM images, as the AFM images are the convolution of the shape of the diamond with the shape of the AFM tip.

are generally shorter in nanodiamond and shallow NVCs than in bulk diamond [34,35,43,44]. The surface effects in this work appear to be significant when compared with a larger diamond of similar substitutional-nitrogen concentration characterized in Ref. [46]. As would be expected, the NVC with the longest Hahn-echo T_2 characterized in that work (which could be up to approximately 100 nm from the diamond surface) has superior $T_2^{(HE)}$ to the NVC defects characterized in this work (which, for ND4, could be up to approximately 5 nm from the surface). This is most likely due to the NVCs in the two works being significantly different distances from the diamond surface. However, by employing a spin-locking pulse sequence, we believe we have demonstrated the longest spin coherence time observed for an NVC in nano- or microdiamond.

Due to the proximity of the NVC in ND4 to the nanodiamond surface, it is likely that there is a contribution to decoherence from charge fluctuations at the surface. Although this has been shown to be a significant source of decoherence for shallow NVCs when $B_\parallel$ is similar to this work [39], it typically only dominates for weaker magnetic fields [40–42]. Electric field noise can drive relaxation between the $m_s = \pm 1$ sublevels, which for near-surface NVCs at low magnetic field can be stronger than the relaxation between the $m_s = 0$ and $m_s = \pm 1$ sublevels [41,42]. The conventional T_1 measured in this work does not provide insight into the relaxation dynamics between the $m_s = \pm 1$ sublevels.

In this study, different NVCs displayed the longest T_2^*, T_2, and T_1 times. This is not necessarily surprising, as different noise sources can dominate the different dephasing and relaxation processes [31,41,65,66]. With the exception of the T_2^* and T_1 measurements for ND5 and ND4, respectively, Fig. 2(d) shows that, in general, the measured times display a consistent pattern between nanodiamonds. Despite ND3 producing longer T_2 times, the T_1 measured for ND4 was longer than that measured for ND3. However, the T_1 measurements for ND3 and ND4 are close and within error. It has been suggested that T_1 is more sensitive to surface spin density than T_2, which could offer a possible explanation as to why the longest recorded T_2 and T_1 were measured for centers in different diamonds [44]. The longest T_2^* was measured for the NVC contained within ND5, which had the lowest measured T_2 and T_1 times of the five NVCs. In general, the measurements for T_2^* do not follow the pattern of the rest of the data. This suggests that the NVCs in different nanodiamonds are subjected to different sources of slowly varying noise (such as magnetic field fluctuations, electric field fluctuations, and strain, among others), which are effectively cancelled by dynamical decoupling, leading to the more uniform pattern observed for the rest of the data.

As NVC sensing techniques are often limited by one or more of T_2^*, T_2, and T_1, as well as how close the NVC can be brought to the target, making these times long for NVCs

in nanodiamond is favorable for many sensing applications [22,67,68]. Furthermore, cellular uptake and biocompatibility have been demonstrated for nanodiamonds similar in size to ND4 [69,70] and so such diamonds are favorable for intracellular sensing techniques [71]. An example is NVC T_1 relaxometry, which has shown promise for detecting free radicals and measuring pH changes in cells, amongst other things [18,67,72–75]. As the sensitivity is limited by the T_1 and proximity to the diamond surface of the NVCs, the availability of smaller diamonds hosting NVCs with longer T_1 offers new opportunities [67,68]. The shortest T_1 measured in this study (1.1 ± 0.1 ms) is comparable to the longest T_1 currently reported in the literature for a single NVC in nanodiamond (1.25 ms) [34].

V. CONCLUSIONS

We have presented long spin-relaxation and -coherence times for single NVCs hosted in nanodiamonds. The nanodiamonds were ball milled with silicon nitride from polycrystalline isotopically purified CVD diamond with an N_s^0 concentration of 0.15 ± 0.02 ppm. The long axis, short axis, and height were measured to be 80 ± 10 nm, 47 ± 10 nm, and 7.8 ± 1.1 nm, respectively, for a particular diamond hosting an NVC found to have $T_2^* = 1.71 \pm 0.20$ µs, $T_2^{(SL)} = 759 \pm 100$ µs, and $T_1 = 4.32 \pm 0.60$ ms. Small diamonds containing NVCs with good spin coherence properties, which can be produced in large quantities, are favorable for a wide variety of sensing applications [18,67,68,72,76,77].

APPENDIX

Figure 4 displays data from EPR measurements taken on the nanodiamond sample. The measurements were made on a 40-mg nanodiamond sample using a Bruker EMX
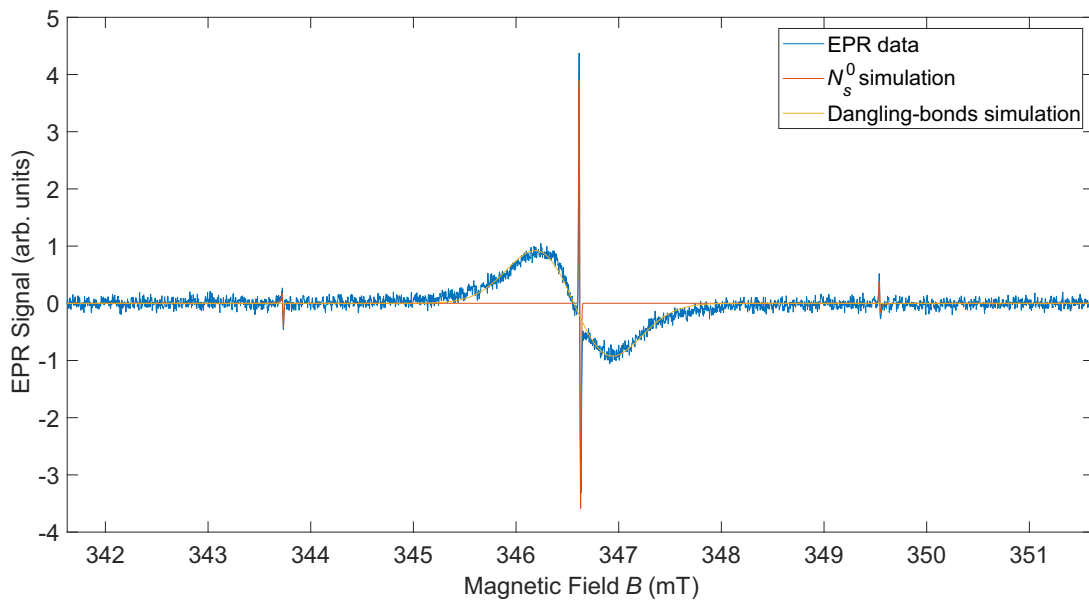
FIG. 4. The EPR data for a 40-mg nanodiamond sample. The blue line shows the EPR data. The red and yellow lines show simulated EPR signals resulting from N_s^0 and dangling bonds, respectively. The simulations were done using EASYSPIN [78]. We find concentrations of 150 ± 15 ppb (parts per billion) and 500 ± 50 ppb for N_s^0 and dangling bonds, respectively.

spectrometer with a Bruker SHQ-E cavity. The modulation frequency and amplitude were 100 kHz and 0.01 mT, respectively. The EASYSPIN software package [78] was used for the data processing and simulations. The EPR data were compared against a well-characterized type-1b diamond and the nanodiamond sample used in this study was found to have an N_s^0 concentration of 150 ± 15 ppb. The EPR signal has a line width of 0.011 mT. We attribute the broad features visible in the spectrum to dangling bonds on the nanodiamond surface, for which we measure a concentration of 500 ± 50 ppb [79–82].

[1] L. Rondin, J.-P. Tetienne, T. Hingant, J.-F. Roch, P. Maletinsky, and V. Jacques, Magnetometry with nitrogen-vacancy defects in diamond, Rep. Prog. Phys. **77,** 056503 (2014).

[2] G. de Lange, D. Ristè, V. V. Dobrovitski, and R. Hanson, Single-spin magnetometry with multipulse sensing sequences, Phys. Rev. Lett. **106,** 080802 (2011).

[3] T. Wolf, P. Neumann, K. Nakamura, H. Sumiya, T. Ohshima, J. Isoya, and J. Wrachtrup, Subpicotesla diamond magnetometry, Phys. Rev. X **5,** 041001 (2015).

[4] M. Loretz, T. Rosskopf, and C. L. Degen, Radio-frequency magnetometry using a single electron spin, Phys. Rev. Lett. **110,** 017602 (2013).

[5] D. M. Toyli, C. F. de las Casas, D. J. Christle, V. V. Dobrovitski, and D. D. Awschalom, Fluorescence thermometry enhanced by the quantum coherence of single spins in diamond, Proc. Natl. Acad. Sci. **110,** 8417 (2013).

[6] G. Kucsko, P. C. Maurer, M. K. N. Y. Yao, H. J. Noh, P. K. Lo, H. Park, and M. D. Lukin, Nanometre-scale

thermometry in a living cell, Nanotechnology **500,** 54 (2013).

[7] S.-C. Zhang, Y. Dong, S. L. B. Du, H.-B. Lin, W. Zhu, X.-D. C. G.-Z. Wang, G.-C. Guo, and F.-W. Sun, A robust fiber-based quantum thermometer coupled with nitrogen-vacancy centers, Rev. Sci. Instrum. **92,** 044904 (2021).

[8] M. Fujiwara and Y. Shikano, Diamond quantum thermometry: From foundations to applications, Nanotechnology **32,** 482002 (2021).

[9] F. Dolde, M. W. Doherty, J. Michl, I. Jakobi, B. Naydenov, S. Pezzagna, J. Meijer, P. Neumann, F. Jelezko, N. B. Manson, and J. Wrachtrup, Nanoscale detection of a single fundamental charge in ambient conditions using the NV^- center in diamond, Phys. Rev. Lett. **112,** 097603 (2014).

[10] E. H. Chen, H. A. Clevenson, K. A. Johnson, L. M. Pham, D. R. Englund, P. R. Hemmer, and D. A. Braje, High-sensitivity spin-based electrometry with an ensemble of nitrogen-vacancy centers in diamond, Phys. Rev. A **95,** 053417 (2017).

[11] R. Li, F. Kong, P. Zhao, Z. Cheng, Z. Qin, M. Wang, Q. Zhang, P. Wang, Y. Wang, F. Shi, and J. Du, Nanoscale electrometry based on a magnetic-field-resistant spin sensor, Phys. Rev. Lett. **124,** 247701 (2020).

[12] P. Wang, Z. Yuan, P. Huang, X. Rong, M. Wang, X. Xu, C. Duan, C. Ju, F. Shi, and J. Du, High-resolution vector microwave magnetometry based on solid-state spins in diamond, Nat. Commun. **6,** 6631 (2015).

[13] S. Nomura, K. Kaida, H. Watanabe, and S. Kashiwaya, Near-field radio-frequency imaging by spin-locking with a nitrogen-vacancy spin sensor, J. Appl. Phys. **130,** 024503 (2021).

[14] M. W. Doherty, N. B. Manson, P. Delaney, F. Jelezko, J. Wrachtrup, and L. C. L. Hollenberg, The nitrogen-vacancy colour centre in diamond, Phys. Rep. **528,** 1 (2013).

[15] V. Vaijayanthimala, P.-Y. Cheng, S.-H. Yeh, K.-K. Liu, C.-H. Hsiao, J.-I. Chao, and H.-C. Chang, The long-term stability and biocompatibility of fluorescent nanodiamond as an *in vivo* contrast agent, Biomaterials **33**, 7794 (2012).

[16] R. Igarashi, Y. Yoshinari, H. Yokota, T. Sugi, F. Sugihara, K. Ikeda, H. Sumiya, S. Tsuji, I. Mori, H. Tochio, Y. Harada, and M. Shirakawa, Real-time background-free selective imaging of fluorescent nanodiamonds in vivo, Nano Lett. **12**, 5726 (2012).

[17] F. P. Martínez, A. C. Nusantara, M. Chipaux, S. K. Padamati, and R. Schirhagl, Nanodiamond relaxometry-based detection of free-radical species when produced in chemical reactions in biologically relevant conditions, ACS Sens. **15**, 3862 (2020).

[18] T. Fujisaku, R. Tanabe, S. Onoda, R. Kubota, T. F. Segawa, F. T.-K. So, T. Ohshima, I. Hamachi, M. Shirakawa, and R. Igarashi, pH nanosensor using electronic spins in diamond, ACS Nano **13**, 11726 (2019).

[19] D. E. J. Waddington, M. Sarracanie, H. Zhang, N. Salameh, D. R. Glenn, E. Rej, T. Gaebel, T. Boele, R. L. Walsworth, D. J. Reilly, and M. S. Rosen, Nanodiamond-enhanced MRI via *in situ* hyperpolarization, Nat. Commun. **8**, 15118 (2017).

[20] B. S. Miller, L. Bezinge, H. D. Gliddon, D. Huang, G. Dold, E. R. Gray, J. Heaney, P. J. Dobson, E. Nastouli, J. J. L. Morton, and R. A. McKendry, Spin-enhanced nanodiamond biosensing for ultrasensitive diagnostics, Nature **587**, 588 (2020).

[21] C.-F. Liu, W.-H. Leong, K. Xia, X. Feng, A. Finkler, A. Denisenko, J. Wrachtrup, Q. Li, and R.-B. Liu, Ultra-sensitive hybrid diamond nanothermometer, Natl. Sci. **8**, nwaa194 (2021).

[22] J. F. Barry, J. M. Schloss, E. Bauch, M. J. Turner, C. A. Hart, L. M. Pham, and R. L. Walsworth, Sensitivity optimization for NV-diamond magnetometry, Rev. Mod. Phys. **92**, 015004 (2020).

[23] R. Li, T. Vedelaar, A. Mzyk, A. Morita, S. K. Padamati, and R. Schirhagl, Following polymer degradation with nanodiamond magnetometry, ACS Sens. **7**, 123 (2022).

[24] J. Barton, M. Gulka, J. Tarabek, Y. Mindarava, Z. Wang, J. Schimer, H. Raabova, J. Bednar, M. B. Plenio, F. Jelezko, M. Nesladek, and P. Cigler, Nanoscale dynamic readout of a chemical redox process using radicals coupled with nitrogen-vacancy centers in nanodiamonds, ACS Nano **14**, 12938 (2020).

[25] J. Holzgrafe, Q. Gu, J. Beitner, D. M. Kara, H. S. Knowles, and M. Atatüre, Nanoscale NMR spectroscopy using nanodiamond quantum sensors, Rev. Rev. App. **13**, 044004 (2020).

[26] Q.-Y. Cao, P.-C. Yang, M.-S. Gong, M. Yu, A. Retzker, M. Plenio, C. Müller, N. Tomek, B. Naydenov, L. McGuinness, F. Jelezko, and J.-M. Cai, Protecting quantum spin coherence of nanodiamonds in living cells, Rev. Rev. App. **13**, 024021 (2020).

[27] M. Scala, M. S. Kim, G. W. Morley, P. F. Barker, and S. Bose, Matter-wave interferometry of a levitated thermal nano-oscillator induced and probed by a spin, Phys. Rev. Lett. **111**, 180403 (2013).

[28] Z.-Q. Yin, T. Li, X. Zhang, and L. M. Duan, Large quantum superpositions of a levitated nanodiamond through spin-optomechanical coupling, Phys. Rev. A **88**, 033614 (2013).

[29] B. D. Wood, S. Bose, and G. W. Morley, Spin dynamical decoupling for generating macroscopic superpositions of a free-falling nanodiamond, Phys. Rev. A **105**, 012824 (2022).

[30] S. Bose, A. Mazumdar, G. W. Morley, H. Ulbricht, M. Toroš, M. Paternostro, A. A. Geraci, P. F. Barker, M. S. Kim, and G. Milburn, Spin entanglement witness for quantum gravity, Phys. Rev. Lett. **119**, 240401 (2017).

[31] T. Rosskopf, A. Dussaux, K. Ohashi, M. Loretz, R. Schirhagl, H. Watanabe, S. Shikata, K. M. Itoh, and C. L. Degen, Investigation of surface magnetic noise by shallow spins in diamond, Phys. Rev. Lett. **112**, 147602 (2014).

[32] C. J. Stephen, B. L. Green, Y. N. D. Lekhai, L. Weng, P. Hill, S. Johnson, A. C. Frangeskou, P. L. Diggle, Y.-C. Chen, M. J. Strain, E. Gu, M. E. Newton, J. M. Smith, P. S. Salter, and G. W. Morley, Deep three-dimensional solid-state qubit arrays with long-lived spin coherence, Phys. Rev. Appl. **12**, 064005 (2019).

[33] G. Balasubramanian, P. Neumann, D. Twitchen, M. Markham, R. Kolesov, N. Mizuochi, J. Isoya, J. Achard, J. Beck, J. Tissler, V. Jacques, P. R. Hemmer, F. Jelezko, and J. Wrachtrup, Ultralong spin coherence time in isotopically engineered diamond, Nat. Mat. **8**, 383 (2009).

[34] H. S. Knowles, D. M. Kara, and M. Atatüre, Observing bulk diamond spin coherence in high-purity nanodiamonds, Nat. Mater. **13**, 21 (2014).

[35] S. Sangtawesin, B. L. Dwyer, S. Srinivasan, J. J. Allred, L. V. H. Rodgers, K. De Greve, A. Stacey, N. Dontschuk, K. M. O'Donnell, D. Hu, D. A. Evans, C. Jaye, D. A. Fischer, M. L. Markham, D. J. Twitchen, H. Park, M. D. Lukin, and N. P. de Leon, Origins of diamond surface noise probed by correlating single-spin measurements with surface spectroscopy, Phys. Rev. X **9**, 031052 (2019).

[36] R. G. Ryan, A. Stacey, K. M. O'Donnell, T. Ohshima, B. C. Johnson, L. C. L. Hollenberg, P. Mulvaney, and D. A. Simpson, Impact of surface functionalization on the quantum coherence of nitrogen-vacancy centers in nanodiamonds, ACS Appl. Mater. Interfaces **10**, 13143 (2018).

[37] T. de Guillebon, B. Vindolet, J.-F. Roch, V. Jacques, and L. Rondin, Temperature dependence of the longitudinal spin relaxation time T_1 of single nitrogen-vacancy centers in nanodiamonds, Phys. Rev. B **102**, 165427 (2020).

[38] U. Zvi, D. R. Candido, A. Weiss, A. R. Jones, L. Chen, I. Golovina, X. Yu, S. Wang, D. V. Talapin, M. E. Flatté, A. P. Esser-Kahn, and P. C. Maurer, Engineering spin coherence in core-shell diamond nanocrystals, ArXiv:2305.03075 (2023).

[39] M. Kim, H. J. Mamin, M. H. Sherwood, K. Ohno, D. D. Awschalom, and D. Rugar, Decoherence of near-surface nitrogen-vacancy centers due to electric field noise, Phys. Rev. Lett. **115**, 087602 (2015).

[40] P. Jamonneau, M. Lesik, J. P. Tetienne, I. Alvizu, L. Mayer, A. Dreau, S. Kosen, J.-F. Roch, S. Pezzagna, J. Meijer, T. Teraji, Y. Kubo, P. Bertet, J. R. Maze, and V. Jacques, Competition between electric field and magnetic field noise in the decoherence of a single spin in diamond, Phys. Rev. B **93**, 024305 (2016).

[41] B. A. Myers, A. Ariyaratne, and A. C. Bleszynski Jayich, Double-quantum spin-relaxation limits to coherence of

near-surface nitrogen-vacancy centers, Phys. Rev. Lett. **118,** 197201 (2017).

[42] A. Gardill, M. C. Cambria, and S. Kolkowitz, Fast relaxation on qutrit transitions of nitrogen-vacancy centers in nanodiamonds, Phys. Rev. Appl. **13,** 034010 (2020).

[43] J.-P. Tetienne, T. Hingant, L. Rondin, A. Cavailles, L. Mayer, G. Dantelle, T. Gacoin, J. Wrachtrup, J.-F. Roch, and V. Jacques, Spin relaxometry of single nitrogen-vacancy defects in diamond nanocrystals for magnetic noise sensing, Phys. Rev. B **87,** 235436 (2013).

[44] X. Song, J. Zhang, F. Feng, J. Wang, W. Zhang, L. Lou, W. Zhu, and G. Wang, A statistical correlation investigation for the role of surface spins to the spin relaxation of nitrogen vacancy centers, AIP Adv. **4,** 047103 (2014).

[45] P. Andrich, B. J. Alemán, J. C. Lee, K. Ohno, C. F. de las Casas, F. J. Heremans, E. L. Hu, and D. D. Awschalom, Engineered micro- and nanoscale diamonds as mobile probes for high-resolution sensing in fluid, Nano Lett. **14,** 4959 (2014).

[46] B. D. Wood, G. A. Stimpson, J. E. March, Y. N. D. Lekhai, C. J. Stephen, B. L. Green, A. C. Frangeskou, L. Ginés, S. Mandal, O. A. Williams, and G. W. Morley, Long spin coherence times of nitrogen vacancy centers in milled nanodiamonds, Phys. Rev. B **105,** 205401 (2022).

[47] M. E. Trusheim, L. Li, A. Laraoui, E. H. Chen, H. Bakhru, T. Schröder, O. Gaathon, C. A. Meriles, and D. Englund, Scalable fabrication of high purity diamond nanocrystals with long-spin coherence nitrogen vacancy centers, Nano Lett. **14,** 32 (2014).

[48] L. Ginés, S. Mandal, D. J. Morgan, R. Lewis, P. R. Davies, P. Borri, G. W. Morley, and O. A. Williams, Production of metal-free diamond nanoparticles, ACS Omega **3,** 16099 (2018).

[49] A. Laraoui and C. A. Meriles, Approach to dark spin cooling in a diamond nanocrystal, ACS Nano **7,** 3403 (2013).

[50] N. Bar-Gill, in *Thermodynamics in the Quantum Regime: Fundamental Aspects and New Directions*, edited by F. Binder, L. Correa, C. Gogolin, J. Anders, and G. Adesso (Springer International Publishing, Cham, 2018), p. 983.

[51] P. Fernández-Acebal, O. Rosolio, J. Scheuer, C. Müller, S. Müller, S. Schmitt, L. McGuinness, I. Schwarz, Q. Chen, A. Retzker, B. Naydenov, F. Jelezko, and M. B. Plenio, Toward hyperpolarization of oil molecules via single nitrogen vacancy centers in diamond, Nano Lett. **18,** 1882 (2018).

[52] J. Scheuer, I. Schwartz, S. Müller, Q. Chen, I. Dhand, M. B. Plenio, B. Naydenov, and F. Jelezko, Robust techniques for polarization and detection of nuclear spin ensembles, Phys. Rev. B **96,** 174436 (2017).

[53] J. M. Binder, A. Stark, N. Tomek, J. Scheuer, F. Frank, K. D. Jahnke, C. Müller, S. Schmitt, M. H. Metsch, T. Unden, T. Gehring, A. Huck, U. L. Andersen, L. J. Rogers, and F. Jelezko, QUDI: A modular PYTHON suite for experiment control and data processing, SoftwareX **6,** 85 (2017).

[54] T. Schröder, F. Gädeke, M. J. Banholzer, and O. Benson, Ultrabright and efficient single-photon generation based on nitrogen-vacancy centres in nanodiamonds on a solid immersion lens, New J. Phys. **13,** 055017 (2011).

[55] L. M. Pham, N. Bar-Gill, C. Belthangady, D. Le Sage, P. Cappellaro, M. D. Lukin, A. Yacoby, and R. L. Walsworth, Enhanced solid-state multispin metrology using dynamical decoupling, Phys. Rev. B **86,** 045214 (2012).

[56] A. M. Souza, G. A. Alvarez, and D. Suter, Effects of time-reversal symmetry in dynamical decoupling, Phys. Rev. A **85,** 032306 (2012).

[57] M. A. Ali Ahmed, G. A. Alvarez, and D. Suter, Robustness of dynamical decoupling sequences, Phys. Rev. A **87,** 042309 (2013).

[58] B. Naydenov, F. Dolde, L. T. Hall, C. Shin, H. Fedder, L. C. L. Hollenberg, F. Jelezko, and J. Wrachtrup, Dynamical decoupling of a single-electron spin at room temperature, Phys. Rev. B **83,** 081201(R) (2011).

[59] S. Claveau, J.-R. Bertrand, and F. Treussart, Fluorescent nanodiamond applications for cellular process sensing and cell tracking, Micromachines **9,** 247 (2018).

[60] E. Bauch, S. Singh, J. Lee, C. A. Hart, J. M. Schloss, M. J. Turner, J. F. Barry, L. M. Pham, N. Bar-Gill, S. F. Yelin, and R. L. Walsworth, Decoherence of ensembles of nitrogen-vacancy centers in diamond, Phys. Rev. B **102,** 134210 (2020).

[61] A. M. Edmonds, *et al.*, Characterisation of CVD diamond with high concentrations of nitrogen for magnetic-field sensing applications, Mater. Quantum. Technol. **1,** 025001 (2021).

[62] N. Mizuochi, P. Neumann, F. Rempp, J. Beck, V. Jacques, P. Siyushev, K. Nakamura, D. J. Twitchen, H. Watanabe, S. Yamasaki, F. Jelezko, and J. Wrachtrup, Coherence of single spins coupled to a nuclear spin bath of varying density, Phys. Rev. B **80,** 041201(R) (2009).

[63] E. Bauch, C. A. Hart, J. M. Schloss, M. J. Turner, J. F. Barry, P. Kehayias, S. Singh, and R. L. Walsworth, Ultralong dephasing times in solid-state spin ensembles via quantum control, Phys. Rev. X **8,** 031025 (2018).

[64] T. A. Kennedy, F. T. Charnock, J. S. Colton, J. E. Butler, R. C. Linares, and P. J. Doering, Single-qubit operations with the nitrogen-vacancy center in diamond, Phys. Status Solids (b) **223,** 416 (2002).

[65] A. Jarmola, V. M. Acosta, K. Jensen, S. Chemerisov, and D. Budker, Relaxation in nitrogen-vacancy ensembles in diamond, Phys. Rev. Lett. **108,** 197601 (2012).

[66] Y. Romach, C. Müller, T. Unden, L. Rogers, T. Isoda, K. Itoh, M. Markham, A. Stacey, J. Meijer, S. Pezzagna, B. Naydenov, L. McGuinness, N. Bar-Gill, and F. Jelezko, Spectroscopy of surface-induced noise using shallow spins in diamond, Phys. Rev. Lett. **114,** 017601 (2015).

[67] A. Myzk, A. Sigaeva, and R. Schirhagl, Relaxometry with nitrogen vacancy (NV) centers in diamond, Acc. Chem. Res. **55,** 3572 (2022).

[68] Y. Wu and T. Weil, Recent developments of nanodiamond quantum sensors for biological applications, Sci. Rep. **9,** 2200059 (2022).

[69] Z. Chu, S. Zhang, B. Zhang, C. Zhang, C.-Y. Fang, I. Rehor, P. Cigler, H.-C. Chang, G. Lin, R. Liu, and Q. Li, Unambiguous observation of shape effects on cellular fate of nanoparticles, Sci. Rep. **4,** 4495 (2014).

[70] M. Chipaux, K. J. van der Laan, S. R. Hemelaar, M. Hasani, T. Zheng, and R. Schirhagl, Nanodiamonds and their applications in cells, Small **14,** 1704263 (2018).

[71] S. Belser, J. Hart, Q. Gu, L. Shanahan, and H. Knowles, Opportunities for diamond quantum metrology in biological systems, Appl. Phys. Lett. **123,** 020501 (2023).

[72] L. Nie, A. C. Nusantara, V. G. Damle, M. V. Baranov, M. Chipaux, C. Reyes-San-Martin, T. Hamoh, C. P. Epperla, M. Guricova, P. Cigler, G. van den Bogaart, and R. Schirhagl, Quantum sensing of free radicals in primary human dendritic cells, Nano Lett. **22,** 1818 (2022).

[73] K. Wu, T. A. Vedelaar, V. G. Damle, A. Morita, J. Mougnaud, C. Reyes-San-Martin, Y. Zhang, D. P. I. van der Pol, H. Ende-Metselaar, I. Rodenhuis-Zybert, and R. Schirhagl, Applying NV center-based quantum sensing to study intracellular free radical response upon viral infections, Redox Biol. **52,** 102279 (2022).

[74] T. Rendler, J. Neburkova, O. Zemek, J. Kotek, A. Zappe, Z. Chu, P. Cigler, and J. Wrachtrup, Optical imaging of localized chemical events using programmable diamond quantum nanosensors, Nat. Commun. **8,** 1470 (2017).

[75] T. Zhang, G. Pramanik, K. Zhang, M. Gulka, L. Wang, J. Jing, F. Xu, Q. W. Z. Li, P. Cigler, and Z. Chu, Toward quantitative bio-sensing with nitrogen-vacancy center in diamond, ACS Sens. **6,** 2077 (2021).

[76] M. Hollendonner, S. Sharma, D. B. R. Dasari, A. Finkler, S. V. Kusminskiy, and R. Nagy, Quantum sensing of electric field distributions of liquid electrolytes with NV-centers in nanodiamonds, New J. Phys. **25,** 093008 (2023).

[77] L. P. McGuinness, L. T. Hall, A. Stacey, D. A. Simpson, C. D. Hill, J. H. Cole, K. Ganesan, B. C. Gibson, S. Prawer, and P. Mulvaney, Ambient nanoscale sensing with single spins using quantum decoherence, New J. Phys. **15,** 073042 (2013).

[78] S. Stoll and A. Schweiger, EASYSPIN, a comprehensive software package for spectral simulation and analysis in epr, J. Magn. Reson. **178,** 42 (2006).

[79] C. Presti, A. S. L. Thankamony, J. G. Alauzun, P. H. Mutin, D. Carnevale, C. Lion, H. Vezin, D. Laurencin, and O. Lafon, NMR and EPR characterization of functionalized nanodiamonds, J. Phys. Chem. **119,** 12408 (2015).

[80] A. M. Panich, A. I. Shames, N. A. Sergeev, M. Olszewski, J. K. McDonough, V. N. Mochalin, and Y. Gogotsi, Nanodiamond graphitization: A magnetic resonance study, J. Phys.: Condens. Matter. **25,** 245303 (2013).

[81] P. I. Belobrov, S. K. Gordeev, E. A. Petrakovskaya, and O. V. Falaleev, Paramagnetic properties of nanodiamond, Dokl. Phys. **46,** 459 (2001).

[82] A. Soltamova, I. Ilyin, P. Baranov, A. Vul, S. Kidalov, F. Shakhov, G. Mamin, S. Orlinskii, N. Silkin, and M. Salakhov, Detection and identification of nitrogen defects in nanodiamond as studied by EPR, Physica B **404,** 4518 (2009).